MECHANICAL BEHAVIOUR OF POLYMERIC LATTICE STRUCTURES PRODUCED BY ADDITIVE MANUFACTURING

A THESIS SUBMITTED TO
THE GRADUATE SCHOOL OF NATURAL AND APPLIED SCIENCES
OF
MIDDLE EAST TECHNICAL UNIVERSITY

BY

ŞÜKRÜ GÜRAY KALAYCIOĞLU

IN PARTIAL FULFILLMENT OF THE REQUIREMENTS
FOR
THE DEGREE OF MASTER OF SCIENCE
IN
MECHANICAL ENGINEERING

NOVEMBER 2022

Approval of the thesis:

MECHANICAL BEHAVIOUR OF POLYMERIC LATTICE STRUCTURES PRODUCED BY ADDITIVE MANUFACTURING

submitted by **ŞÜKRÜ GÜRAY KALAYCIOĞLU** in partial fulfillment of the requirements for the degree of **Master of Science in Mechanical Engineering, Middle East Technical University** by,

Prof. Dr. Halil Kalıpçılar
Dean, Graduate School of **Natural and Applied Sciences** _____

Prof. Dr. M. A. Sahir Arıkan
Head of the Department, **Mechanical Engineering** _____

Assoc. Prof. Dr. Sezer Özerinç
Supervisor, **Mechanical Engineering, METU** _____

Examining Committee Members:

Assoc. Prof. Dr. Kıvanç Azgın
Mechanical Engineering, METU _____

Assoc. Prof. Dr. Sezer Özerinç
Mechanical Engineering, METU _____

Assoc. Prof. Dr. Ulaş Yaman
Mechanical Engineering, METU _____

Assoc. Prof. Dr. Ender Yıldırım
Mechanical Engineering, METU _____

Assoc. Prof. Dr. Recep Muhammet Görgülüarslan
Mechanical Engineering, TOBB ETÜ _____

Date: 25.11.2022

I hereby declare that all information in this document has been obtained and presented in accordance with academic rules and ethical conduct. I also declare that, as required by these rules and conduct, I have fully cited and referenced all material and results that are not original to this work.

Name Last Name : Şükrü Güray Kalaycıoğlu

Signature :

ABSTRACT

MECHANICAL BEHAVIOUR OF POLYMERIC LATTICE STRUCTURES PRODUCED BY ADDITIVE MANUFACTURING

Kalaycıoğlu, Şükrü Güray
Master of Science, Mechanical Engineering
Supervisor: Assoc. Prof. Dr. Sezer Özerinç

November 2022, 50 pages

Additive manufacturing (AM) is a manufacturing method based on the layer-by-layer deposition of the desired geometry. Polymer AM provides means to produce compliant polymeric structures for impact-absorbing applications. The recent introduction of foaming elastomeric filaments opened a new design space for achieving optimized impact absorbance performance. This thesis investigates this route through the mechanical testing of solid and cellular polymer foam structures produced by additive manufacturing.

The experimental work in this thesis employs Fused Filament Fabrication (FFF), which is a cost-effective AM technique for the rapid manufacturing of complicated geometries in low quantities. Recent advances in filament technology have enabled the production of foaming thermoplastic polyurethane (TPU) filaments, which makes the printing of microporous polymeric structures possible through the FFF method.

The first part of the thesis investigates the mechanical properties of the TPU foam produced by FFF. The systematic experiments show that the nozzle temperature directly influences the foaming behavior. With increasing temperature, the extent of foaming increases, which results in a decrease in the elastic modulus and strength.

The second part of the thesis investigates the impact-absorbing performance of honeycomb lattice structures produced by the same foaming TPU. The experiments show that as the nozzle temperature increases, the energy absorption capacity and the peak stress of the lattice structure increase.

Overall, the results demonstrate the great potential of foaming filaments in achieving unique impact-absorbing behavior. Future work will focus on understanding the behavior of different cellular structures and lattice geometries made of TPU foams under load.

Keywords: Additive Manufacturing, Fused Filament Fabrication, 3D Printing, Thermoplastic Polyurethane, Mechanical Properties, Foaming Polymers, Lattice Structures, Energy Absorption

ÖZ

EKLEMELİ İMALAT İLE ÜRETİLEN POLİMER KAFES YAPILARIN MEKANİK DAVRANIŞI

Kalaycıoğlu, Şükrü Güray
Yüksek Lisans, Makina Mühendisliği
Tez Yöneticisi: Doç. Dr. Sezer Özerinç

Kasım 2022, 50 sayfa

Eklemeli imalat, istenen geometrinin katman katman biriktirilmesine dayalı bir üretim yöntemidir. Polimer eklemeli imalatı, darbe emici uygulamalar için uyumlu polimerik yapılar üretmek için yapılar sağlar. Son zamanlarda köpüren elastomerik filamanların piyasaya sürülmesi, optimize edilmiş darbe emme performansı elde etmek için yeni bir tasarım alanı açtı. Bu tez, eklemeli imalatla üretilen katı ve hücresel polimer köpük yapılarının mekanik testi yoluyla bu yolu araştırıyor.

Bu tezdeki deneysel çalışmada, düşük miktarlarda karmaşık geometrilerin hızlı üretimi için uygun maliyetli bir eklemeli imalat tekniği olan Eriyik Yığma Modellemesi (FFF) kullanılmıştır. Filament teknolojisindeki son gelişmeler, FFF yöntemiyle mikro gözenekli polimerik yapıların basılmasını mümkün kılan köpüren termoplastik poliüretan (TPU) filamentlerin üretimini mümkün kılmıştır.

Tezin ilk bölümünde FFF tarafından üretilen TPU köpüğün mekanik özellikleri incelenmiştir. Sistematik deneyler, nozül sıcaklığının, köpürme davranışını doğrudan etkilediğini göstermektedir. Artan sıcaklıkla birlikte, köpürme derecesi artar, bu da elastik modül ve mukavemette bir azalma ile sonuçlanır.

Tezin ikinci kısmı, aynı köpüren TPU'dan üretilen petek kafes yapıların darbe sönümleme performansını araştırmaktadır. Deneyler, nozül sıcaklığı arttıkça, enerji emme kapasitesinin ve kafes yapısının tepe geriliminin arttığını göstermektedir.

Genel olarak sonuçlar, benzersiz darbe emici davranış elde etmede, filamanların köpürmesinin büyük potansiyelini göstermektedir. Gelecekteki çalışmalar, yük altında TPU köpüklerinden yapılmış farklı hücresel yapıların ve kafes geometrilerinin davranışını anlamaya odaklanacaktır.

Anahtar Kelimeler: Eklemeli İmalat, Eriyik Yığma Modellemesi, Termoplastik Poliüretan, 3 Boyutlu Baskı, Mekanik Özellikler, Köpüren Polimerler, Kafes Yapılar, Enerji Emicilik

To My Family

ACKNOWLEDGMENTS

I would like to thank my supervisor Assoc. Prof. Sezer Özerinç for his guidance and priceless support to encourage me during my thesis study. I am grateful to him for his precious recommendations and guidance that helps me to improve myself.

I want to thank Servet Şehirli for his help to able to finish my study. Also, I want to thank Nanomechanics Labarotary members, especially Roozbeh Neshani, Amir Fadaie, Mehmet Kepenekçi and Çağla Melis Aslan for their collaboration, encouraging supports, sharing information and experiences, suggestions and friendship.

I would like to thank Ali Güzel and the METU Central Laboratory staff for their help.

I want to thank my colleagues, work team and lead engineer. They always support and encourage me during my study.

I want to thank my friends who always support and motivate me to proceed during my study.

Lastly, I want to thank my family for their endless support and motivation to finish my thesis study. I cannot complete this study without their support.

TABLE OF CONTENTS

LIST OF TABLES

LIST OF FIGURES

LIST OF ABBREVIATIONS

ABBREVIATIONS

TM	Traditional Manufacturing
AM	Additive Manufacturing
DFM	Design for Manufacturing
DFA	Design for Assembly
SLA	Stereolithography
SLS	Selective Laser Sintering
FDM	Fused Deposition Modeling
FFF	Fused Filament Fabrication
LMD	Laser Material Deposition
PA	Polyamide
PEEk	Polyetheretherketone
CAD	Computer Aided Design
STL	Stereolithography File
TPE	Thermoplastic Elastomer
ABS	Acrylonitrile Butadiene Styrene
PLA	Polylactic Acid
TPU	Thermoplastic Polyurethane
3D	Three Dimensional
LW	Light Weight

CHAPTER 1

INTRODUCTION

1.1 Overview

Additive manufacturing (AM) is creating a three-dimensional object from a CAD model by arranging manufacturing parameters as desired and by laying down layers upon each other [1]. This technology was born in the 1980s due to the necessity of creating models before the final product and prototyping [2]. AM allows to creation desired part in a limited time. Also, before finalizing the geometry, it is possible to see the usefulness of the part. So, it is beneficial to reduce manufacturing costs and improve the product cycle. Besides, AM enables the creation of complex geometries which is not possible with traditional manufacturing (TM). This brings the design for manufacturing and assembly (DFM/DFA). Considering the capabilities of AM, more advanced final products are becoming easier to create such as optimized geometries or one-piece geometries without assembly needed. This situation also reduced material and energy waste. Compared to AM, TM wastes more material and needs a product-specific assembly line [3].

AM meets environmental and economical concerns. This approach shows that AM has an obvious supremacy over TM. However, it is not. Both manufacturing techniques have advantages and disadvantages. The main idea is to define a trade-off between the AM and the TM and replace TM when it is possible [4]. Thus, the negative effects of TM on the environment and the cost can be reduced.

AM includes a wide range of techniques. Mahamood et al. [5] classified these techniques into two main parts, first laser additive manufacturing such as stereolithography (SLA), selective laser sintering (SLS), laser binging, and laser material deposition (LMD), second non-laser based additive manufacturing such as

ink-jet printing, fused deposition modeling (FDM) and infrared and masking systems.

FDM is one of the most popular AM techniques, also known as fused filament fabrication (FFF). The reason is that it is easy to achieve, easy to use, and does not contain any chemical process compared to other AM methods. The feed material has considerably cheap prices and it is small in size. It uses a filament that is wrapped into a spool. This spool feeds the FDM machine that has a heated nozzle. The nozzle melts the material and then extrudes it on a preheated plate. Material is fused layer by layer while following a predefined path. This path is generated from a stereolithography file (STL) [6].

Common properties of FFF materials are making strong bonding between layers at their melting points and when the temperature of the melted material turns back to room temperature, layers are solidified and should not have insufficient residual stress [7]. Polylactic acid (PLA) and acrylonitrile butadiene styrene (ABS) are common materials for the FFF. However, the thermoplastic material is also used as material for the FFF. PLA and ABS are more user-friendly materials and easy to print.

In this thesis study, foamed TPU was used in changing extrusion temperature. First, the tensile and the compression specimens were printed, and tests were performed to obtain the mechanical properties of foamed TPU at different printing temperatures. Then, honeycomb structures were printed with the same procedure and different nozzle temperatures. Compression tests were performed to obtain the energy absorption levels of honeycomb structures.

1.2 Fused Filament Fabrication

Fused filament fabrication (FFF) is one of the most widely used AM techniques. It is also known as fused deposition modeling (FDM). Steven Scott Crump from Stratasys is the pioneer of this technology. He developed FFF in 1989 [8]. FFF

started as research purposes manufacturing device; however, it is not limited to only research purposes. The FFF is used in engineering, science, prototyping, and industrial purposes [9]. FFF allows changing various manufacturing parameters and is available to create custom-shaped products. These specialties make FFF irreplaceable among other AM techniques. FFF covers %69 of all AM techniques. Even if FFF does not have the best finalized material properties, in many applications, FFF is preferred to apply desired parameters [10].

There are different types of FFF in the industry. However, their working principle is the same. The working principle can be generalized as extruding the material to a repeated layer and making one finalized geometry on a print bed [10], [13].

The printing process starts with preparing of CAD model of the necessary product. Then, the CAD file should be converted into printer-readable form and sliced. After slicing, printing layers are built up for FFF. The path of creating layer sequences is introduced with G-code to a machine. G-code has information on the movement of a nozzle in the XY plane. After creating one layer, the print bed moves in the Z direction to create the next layer over the previous one geometry is finalized [12].

During the manufacturing process, the printing mechanism showed in Figure 1.1. The FFF process can be divided into three main parts extrusion, fusion, and solidification. [11]. The first material filament is loaded to FFF and then will enter the extrusion chamber, which should be heated first to make liquid the filament. The molten filament can extrude to the print bed through a nozzle. The nozzle diameter directly affects the print quality. The second phase is material interaction between the print bed and the layers. The material should not have residual stress to cause any delamination. The final phase is the solidification. During the solidification, the product layers should protect the shape and size of the geometry. Gravity and the surface tension, the cooling rate, and the temperature gradient affect the solidification. So, it should be careful to prevent unwanted effects [13], [15], [16].

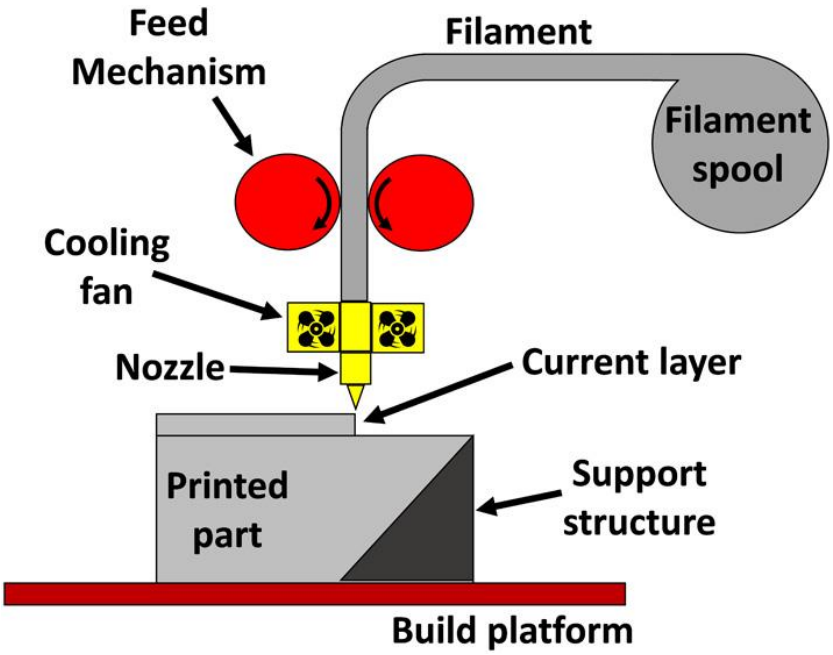

Figure 1.1 Schematic of FFF printing machine [15].

1.3 FFF Materials

Nowadays, FFF has a large variety of filament materials. As the usage of the FFF area increases, different materials are beginning to integrate into FFF printers. The most common printing materials are acrylonitrile butadiene styrene (ABS) and polylactic acid (PLA) for FFF [16]. Materials in FFF are required to be softened and show low viscosity by heating up. Therefore, thermoplastics are also suitable materials for the FFF technique. There are lots of thermoplastics available as filament materials used in engineering applications; they are PA, TPU, PEEk, and PEI. PLA and ABS are more user-friendly materials. They are easy to print and reachable to any user. However, to print engineering materials, users should deal with lots of problems. Table 1.1 shows the average mechanical properties of commercially available filament materials [15].

Table 1.1 Bulk mechanical properties of conventional thermoplastic filaments [15].

Polymer	Yield Strength (MPa)	Tensile Strength (MPa)	Elastic Modulus (GPa)	Elongation at Break (%)
ABS	35–58	25–65	1.9–2.7	8–20
Nylon (PA6)	36–95	74–106	0.78–3.8	10–160
PEEK	65–95	75–100	3.5–4.4	20–50
PET	36–63	24–41	2.3	100–250
PLA	66–77	52–72	2.7–16	4–6
TPU	39–54	17–66	0.12–0.33	300–1500

1.4 Elastomers

Elastomers are distinctive materials that have elastic and viscous properties at the same time. Therefore, it is classified as a viscoelastic material. Elastomers have low elastic modulus and high elasticity. It allows elastomers to reach high deflection levels; after the load application is removed, it can save the initial geometry. Elastomers give good results under dynamic loading, they can resist environmental effects and have low compressibility. These properties of elastomers make them a good choice for vibration and impact isolation applications [17], [18]. However, the prediction of the vibration response of elastomeric material is only possible with the identification of the system accurately. The theory of viscoelasticity shows that at least two parameters should be known to identify the mechanical properties of elastomers. These two parameters are generally the Poisson's ratio and one of the moduli of the elastomer [19], [20].

As mentioned before, elastomers have low compressibility which means they are incompressible materials. They change geometric shapes while their volume stays constant. Their Poisson’s ratio is approximately 0.5. Hooke’s law is applicable for low strain values, and the stress-strain curve goes proportional at low strain levels for tension or compression. However, the proportionality breaks at some point when

strain values become relatively high. At this state, the material becomes viscoelastic and Hooke's law is no longer valid [17], [21].

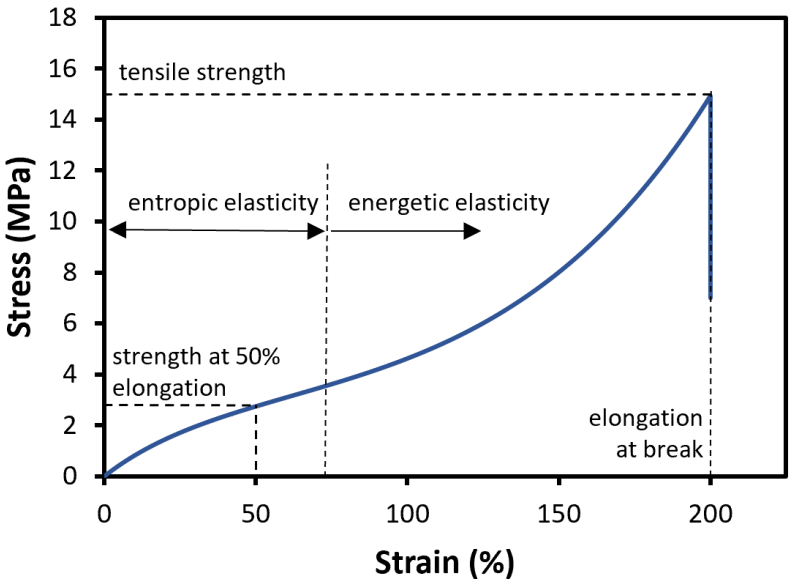

Figure 1.2 Stress-strain behavior of an elastomeric specimen under tension [22].

Figure 1.2 shows the stress-strain behavior of an elastomeric specimen under tension loading. The stress-strain graph shows nonlinear behavior. The graph follows an elastic path initially at small strain levels. This region is valid for Hooke's Law. The tangent line can be drawn to obtain elastic modulus. After proportionality breaks, the curve follows viscoelastic behavior, and there is a smooth transition from elastic behavior to plastic behavior.

Different kinds of elastomeric material show similar mechanical behavior in various application areas. The elastomer can be divided into two groups: first, the conventional or thermoset elastomers, and second, the thermoplastic elastomers [23]. Thermoset elastomers can be defined as cured and shaped polymers. After curing, polymers are crosslinked with chemical bonds. Because of chemical reactions, it is not possible to break bonds. Through crosslinking, thermosets show elastomeric recoverability [24]. Thermoplastic elastomers can be defined as a composition of thermoplastics and elastomers. The structure consists of copolymer blocks which are

ordered as A-B-A. A represents thermoplastic and B represents elastomer [25]. A and B's contribution amount affects the mechanical properties of TPEs.

TPEs are new material and have recently taken place in research areas. It is a unique material because they have a significant deflection level and processing is relatively easy, thanks to microphase separation between copolymer blocks [26]. TPEs' physical crosslink networks can be ripped during the thermal treatments and this allows for physical foaming of TPEs [26].

There are various types of TPE materials which are produced by mixing of two polymer types and produced by block copolymerization of two or more segments of molecularly different polymers. One of the most popular TPE used in daily life and produced by block copolymerization material is TPU [27]. It contains hard and soft segments in the microstructure. Hard segments connected with hydrogen link to each other, and the foaming structure highly depend on to melting of hard and soft segments' architecture [26], [28]. This bonding helps TPU to display high flexibility, elasticity, and shock absorbance characteristics [29]. The material properties can be customized by controlling the ratio of soft and hard segments and structural morphologies [30].

1.5 Foaming Elastomers

The conventional foaming method creates space inside the material and allows it to fill with a gas such as carbon dioxide or nitrogen during the melting process in a controlled pressure medium. Foaming may also be produced by mixing a chemical foaming agent with melted polymer. The main idea is to create bubbles in the polymer structure, then stabilize them to create cellular structure [28], [31], [32]. The porous structure provides space for cell walls to bend and buckle to improve deformability [33]. They were invented to reduce polymer consumption in processes, improve damage tolerance, and increase product's energy absorption and hardness. They are widely used in the aerospace industry, automotive industry, marine and

civil engineering applications due to their market availability, ease of processibility, and strength-to-weight ratio [32], [34].

The conventional methods for the foam manufacturing are only partially successful for the hierarchical structure production and fine control of porosity gradient [35]. Most of the products manufactured with the conventional methods are open-cell structures that are softer and less strong than closed-cell foams. It is not fully effective and easy to produce complex cellular structures with the conventional methods [34]. However, recent studies show that additive manufacturing has a great potential to create cellular structures by controlling internal porous morphology and complex final geometry [31], [35]–[37]. Compared to the random foaming characteristics of the conventional methods, additively manufactured foams have well-defined repeated cell structure, shape, size, and density [31]. Foaming with AM can be classified into four groups. First, architected porous structures, second, synthetic foaming, third, post foaming of printed parts and fourth, printing with foaming agents saturated filaments [38].

Fused filament fabrication is one of the most common methods in AM due to simplicity, relatively low process temperature, controllable fusion and solidification segments and wide range of polymer filaments [34], [39]. As mentioned before, even if FFF is the most common printer, it is still uncovered. ABS and PLA represent %80 of literature work [39]. Recently, attention for elastomer foams with FFF, a less known area, increased.

Elastomers can be foamed by FFF with different techniques for different applications. They can be produced by activating foaming agents [40] or by exposing CO_2 in a controlled temperature and pressure environment [41]. Also, they can be produced by syntactic foaming [42] and architected porous structures [43]. In literature, there are studies such as comparison of foaming at different printing speeds at high temperatures [31], comparison of different percentages of foaming agent and elastomer compounds [44], comparison of CO_2 saturated filaments with

different printing speed and temperatures [45], and comparison of elastomers contains different amounts of thermally expandable microspheres [34].

In this study, elastomers at different printing temperatures were investigated. The main purpose was to make a comparison between the tensile properties and the compression properties of solid specimens. Then, the mechanical properties were defined. After the mechanical properties were defined, the lattice structure properties under the compression of foamed elastomers which were extruded at different temperatures would be investigated. The TPU was selected as elastomer, and Varioshore TPU filament (Colorfabb, Netherlands) was used as filament material which has a chemical foaming agent. The FFF printing method was used in this study since the FFF is suitable for this study to activate the foaming agent and to create controlled porosity by changing the temperature [46]. Moreover, the distribution of hard and soft segments of TPU can be rearranged by extruding at different temperatures [47].

The high flexibility, elasticity and shock absorbance characteristics of TPU take the industry's attention and soft TPU filaments for FFF are started to be produced [48]. TPU can be produced with different grades of thermally expendable microstructures to activate foaming at different temperature levels [34], [49]. By changing the temperature, microstructure can be arranged as desired and foaming starts. The printed materials become anisotropic due to random orientation of particles after the vulcanization of TPU in the three dimensional space [50]. Yet, this makes density control more challenging. Studies showed that additively manufactured polyurethane foams present similar resilience behaviors with bulk rubber material with four-time lower densities [51].

Nowadays, TPU foams have a wide range of applications automotive, electronics, footwear, aerospace, and toys. Insufficient traditional methods increase the attention over additively manufactured TPU foams. Moreover, researchers are investigating the recycling of TPU foams, bio-based TPU foams such as a vegetable-oil-based

polyol, personal protection equipment, electromagnetic interface shielding, sensors, and biomedical usage of TPU [51]–[55].

1.6 Foaming Filaments for FFF Applications

Recently, interest in low-density materials such as porous polymeric structures in FFF is increasing because they show improved thermal, mechanical, and physical properties [56].

Among all foaming methods which are discussed previously, foaming agent activation was investigated in this study. The reason is that commercial foaming filaments are available in the market, and it is easy to process because there is no pre or post-application addition to the printing process. Changing the nozzle temperature, the infill percentage or the flow rate, makes it is easy to activate foaming and obtain a lightweight printed product. Studies show that there are few options for foaming filament to use in FFF printers.

PLA gets attention nowadays and lightweight PLA(LW-PLA) is investigated as foaming filament in literature [56]–[58]. LW-PLA has a chemical foaming agent which requires a certain condition for the activation of foaming material. By foaming, low-density, low weight, and low hardness material are obtained. LW-PLA is used for medical applications, such as creating bone simulant structures [59] or soft tissues [60] and small industrial applications such as creating lightweight brushless motor components [61].

In this study, like LW-PLA, foaming TPU filament, Varioshore TPU is used and by changing the nozzle temperature, different level of foaming was observed and investigated. There are similar studies that investigate different types of foaming TPU materials such as investigating the different compositions of chemical agents and TPU material [62], cell morphology and expansion ratio [40], foaming the printed specimen with CO_2 saturation [41], the compression behavior of star-shaped scaffolds [63], [64], customized crutch grips [65]. In the following sections of this

study, the mechanical properties of foaming TPU at different levels of foaming and the effects of mechanical properties of honeycomb structures are investigated.

CHAPTER 2

EXPERIMENTAL DETAILS

2.1 Overview

In this work, parts printed using Varioshore TPU filament (Colorfabb, Netherlands) was investigated to observe the material properties under different nozzle temperatures. First, the dog bone tensile specimens and the cylinder compression specimens were printed by an Ultimaker 2+ FFF printer. Then, standardized mechanical tests were performed. Second, honeycomb lattice structures were designed and printed. Lastly, the compression tests were performed on these honeycombs to determine their impact-absorbing behavior.

Three identical specimens were manufactured at five different nozzle temperatures for both the tension and the compression experiments. For the honeycomb compression test, six honeycomb structures were manufactured at five different temperatures. In total, sixty samples are manufactured for the experiments. In Table 2.1, the summary of the experiment details is given.

Table 2.1 A summary of experiment details of specimens.

Test	Specimen Geometry	Testing Standard	Number of Samples Tested
Tension	Dog bone Type C (Figure 2.2)	ASTM D412	15
Compression	Cylinder (Figure 2.2)	ASTM D575	15
Lattice compression	Lattice structures (Figure 2.3)	ASTM D1621	30

The tensile specimens were also scanned in SEM to find out the microstructures and porosity levels of specimens.

2.2 Material and Manufacturing

2.2.1 Material

For all samples, CAD models were prepared, then a toolpath was generated with a suitable preprocess program and then samples were printed as finalized products. All products were printed FFF method with Ultimaker 2+ (Ultimaker ltd., Netherlands). Only the extrusion nozzle temperatures were varied.

2.2.2 Modeling and G-Code Generation

At the beginning of the design process, design parameters were decided. According to these parameters, geometries were created. These parameters were discussed in the previous section for 3D modeling of the samples; Solidworks 2020 (Dassault Systems, USA) is used CAD program.

After the modeling phase, able to print finalized geometries, 3D models should be introduced to the printer via G-code. G-code contains toolpath information that the nozzle follows during operation. CAD program gives the STL file as output. The surface of the geometry is split into triangle meshes. STL file is the input of the slicing software to generate the necessary G-code. Open-source software Ultimaker CURA (Ultimaker ltd., Netherlands) was used as slicing software.

2.2.3 Printing Process

As mentioned before, Ultimaker 2+ (Ultimaker ltd., Netherlands) printer was used for this thesis study. The printer is shown in Figure 2.1. It has a single nozzle. Temperature can be arranged between 180°C and 260°C, which is just perfect for

investigated temperatures of this study. The nozzle can be heated up under 2 minutes. Moreover, during the operation, it is observed that the nozzle temperature does not fluctuate excessively. For these reasons, Ultimaker 2+ is reliable for this study.

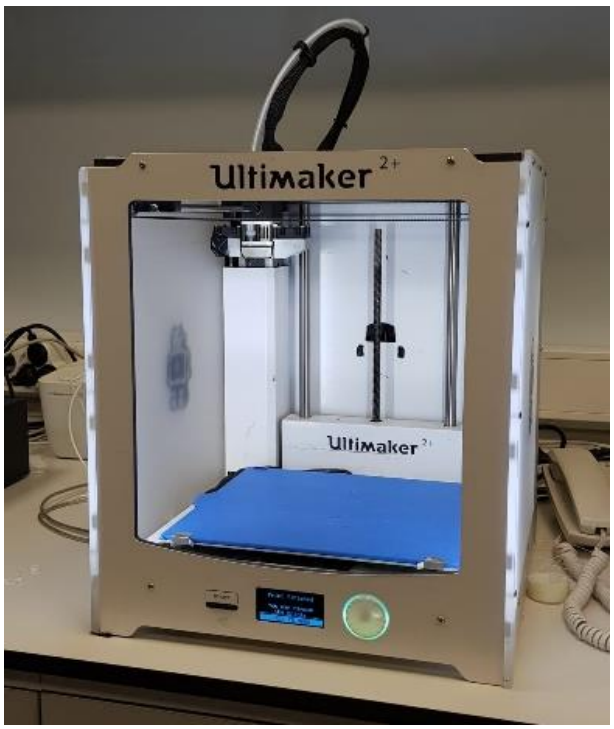

Figure 2.1 Ultimaker 2+ FFF Printer.

According to the specified parameters, the printing process was performed. The tensile and the compression specimens were printed at the same time for the same temperature level, and six honeycomb specimens were printed at the same time for the same temperature. An attempt was made to reduce the deviation in properties to zero.

2.3 Design of Experiments

2.3.1 Tensile and Compression Specimens

The tension test specimens were made according to the D412-16 Type C standard [66]. The compression test specimens were made according to the D575-91 [67].

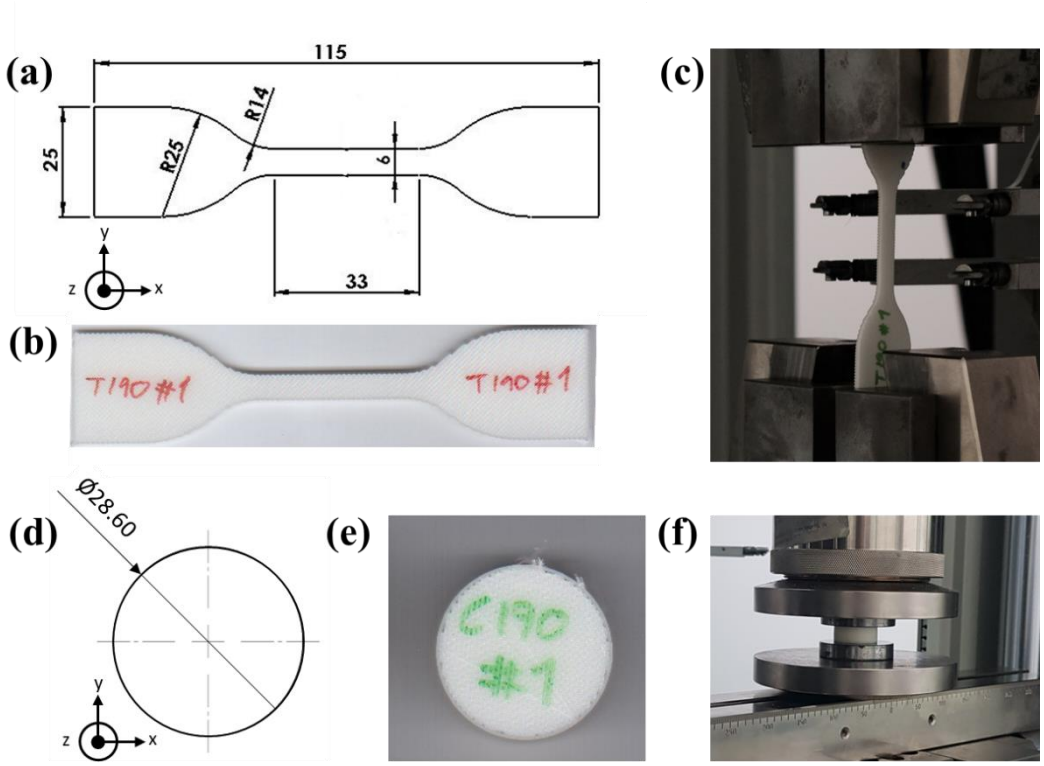

Figure 2.2 (a) Technical drawing of tensile test specimen. (b) A photograph of tensile test specimen. (c) A Photograph of tensile test setup. (d) Technical drawing of compressive test specimen. (e) A photograph of compressive test specimen. (f) A Photograph of compressive test setup. Thicknesses are 3 mm for the tensile test specimens and 12.5 mm for the compression test specimen.

In Figure 2.1 (a) and Figure 2.1 (d), the specimen size for the tension and the compression is given. Figure 2.1 (b) and Figure 2.1 (e) show the manufactured specimens. Manufactured specimen dimensions were in ±0.3% as specified in standards. The dimensions were measured with a caliper, and the room temperature was maintained at 23±2°C during experiments.

The tension and the compression tests were performed in Zwick/Roell Z250 (Germany) universal testing machine (UTM). The tension test speed was 500mm/min. The compression test speed was arranged as 10% of the specimen height was compressed in a minute. In Figure 2.1 (e) and Figure 2.1 (f), the tension and the compression test setups are given. In tension, setup 0.1kN load capacity cell, and in the compression test setup 10kN load capacity cell was used.

All specimens were printed in the Z direction. The system axis is shown in Figure 2.2.

2.3.2 Honeycomb Structures

The lattice structure was designed as honeycomb geometry. The honeycomb structure contains sixty-eight cells whose dimensions are given in Figure 2.3 (a). The height of the honeycomb lattice is 29.5mm. Figure 2.3 (b) shows the printed specimen of the honeycomb. Figure 2.3 (c) shows the test setup. The test was performed with 10kN load capacity cell, and the test speed was arranged according to %10 of the height of the specimen.

Honeycomb specimens printed in the Z direction are shown in Figure 2.3.

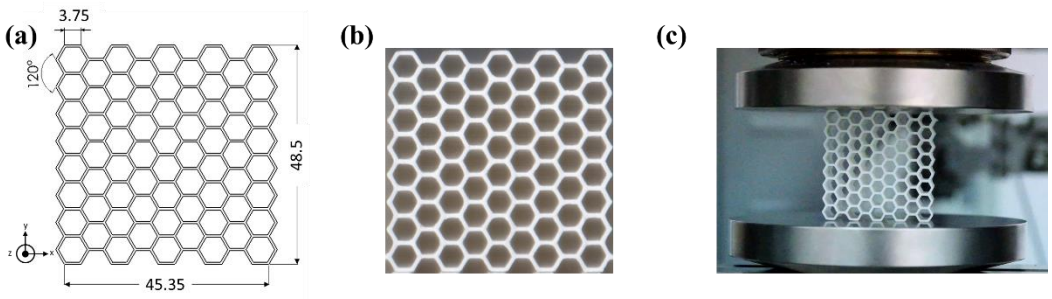

Figure 2.3 (a) Technical Drawing of Honeycomb Specimen. (b) A Photograph of Honeycomb Test Specimen. (c) A Photograph of Honeycomb Compression Test Setup.

2.3.3 Printing Parameters

In Table 2.2, common printer parameters are given, and all experimental procedures were carried out according to these parameters. As noticed, the filament diameter, the nozzle diameter, the layer thickness, the printing speed, the bed temperature, the infill direction and percentage were fixed for the entire experimental setup. These values were recommended values from the technical data sheet (TDS). Only, the

printing temperature was changed. TDS states that the onset of foaming is around 230°C [68]. Detailed parameters for each specimen are given in Appendix A.1.

Table 2.2 Printer Parameters.

Parameters	Values
Filament Diameter [mm]	2.85
Nozzle Diameter [mm]	0.4
Layer Thickness [mm]	0.2
Printing Speed [mm/s]	30
Nozzle Temperature [°C]	190, 205, 220, 235, 250
Bed Temperature	40
Infill Direction	±45°
Infill Percentage	100%

The tensile and the compression test specimens with the same extrusion temperatures were printed in the same operation. Also, the honeycomb structures with the same extrusion temperature were printed in the same operation. The printed products would have better quality if they were printed one by one. However, by arranging toolpath and CAD data, the same quality could be provided. Also, multiple productions at the same time were more time efficient.

The infill direction affects the mechanical properties of structures. To obtain homogenous stress distribution between the layers the infill direction was selected as ±45° [15]. Yet, it was not valid for the honeycomb structures because their wall thickness is 0.2 mm. On the contrary, it was important for the tensile and the compression test specimens. It was expected to behave close to isotropic material since the raster angle was selected as ±45° and the infill percentage is 100%.

2.4 Characterization and Testing

2.4.1 Mechanical Testing

To be able to understand the mechanical properties of the Varioshore TPU filament (Colorfabb, Netherlands), mechanical testing was performed. Since it is novel material, there is not enough study in literature. In this case, it was a big advantage to perform the tensile and the compression tests to validate and compare the literature data and to have a well understanding of the material characteristic.

2.4.1.1 Tensile Testing

At room temperature, uniaxial tensile tests were performed using a uniaxial material testing apparatus (Z250, Zwick/Roell, Germany). As stated in standard D412-16 [66], the test speed was determined as 500 mm/min. 1 N preload was applied to prevent loose of the specimen. The gauge length was specified as 25 mm.

The tensile stress was calculated using the following Equation 2.1.

$$\sigma_t = \frac{F_t}{Ac} \tag{2.1}$$

Here σ_t is the tensile stress, F_t is the applied axial load and A_c is the area of the cross-section.

2.4.1.2 Compression Testing

At room temperature, uniaxial compression tests were performed using a uniaxial material testing apparatus (Z250, Zwick/Roell, Germany). As stated in D575-91 [67] the testing speed was arranged as 10% of specimen height. 10 kN load cell was used to able to complete the experiment. A water gauge was used to ensure uniaxial loading because of the universal joint connection of the load cell to the machine.

The compression stress was calculated using the following Equation 2.2.

$$\sigma_c = \frac{F_c}{Ac} \tag{2.2}$$

Here σ_c is the compression stress, F_c is the applied axial load and A_c is the area of cross-section.

2.4.1.3 Honeycomb Compression Testing

The honeycomb compression test followed the same procedure in the same testing machine with the compression testing. The test speed was determined by 10% of the specimen height. However, there were two possible directions to performing the compression tests. In this study, the X1 direction was preferred to the compression direction, which is shown in Figure 2.4. The scanned area in Figure 2.4 shows the cross-section area which was used in Equation 2.2 for the honeycomb compression stress calculation.

Figure 2.4 (b) showed that the compression test was also applied in the X2 direction for one specimen in each nozzle temperature to find out any difference in mechanical properties. However, it was clarified that there were not any notable differences between the compression load-strain curves. After showing that, the X1 direction was chosen. A detailed comparison of X1 and X2 directions is given in Appendix A.2.

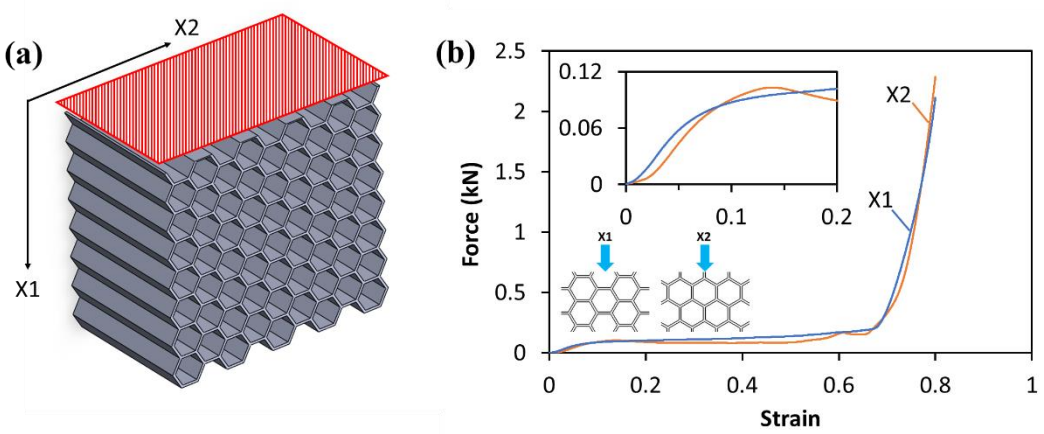

Figure 2.4 (a) Honeycomb test specimen and load directions. (b) Force-Strain curve of loading in X1 and X2 directions of 235^{o}C.

2.4.2 Scanning Electron Microscopy

The tensile test specimens after failure were prepared for the SEM process. This process was necessary to investigate the microstructure and the porosity of the printed specimens at different temperatures. QUANTA 400F Field Emission SEM was used for scanning. It allows high-quality pictures at different levels of zoom.

Failed cross-sections of the tensile specimens were coated with gold, and then scanning was completed for five different temperatures.

CHAPTER 3

RESULTS AND DISCUSSION

In this section of the thesis, the experimental results were discussed. First, tensile test results, then the compression test results were evaluated. The mechanical behavior of Varioshore TPU filament and the printing parameters' effects tried to be figured out. Finally, the honeycomb compression test results were discussed and the energy absorption characteristics and related phenomena were tried to understand.

3.1 Tensile Testing

The Varioshore TPU filament was applied tensile test in five different temperature groups from 190°C to 250°C for a better understanding of the tensile characteristics and the effect of the nozzle temperature during and after the printing process.

Figure 3.1 (a) shows the repeatability of engineering stress-strain data at 235°C. It can be easily seen that the filament material shows the same characteristic at the same extrusion temperature. The tensile specimens stretched until the failure. All specimens start with elastic behavior and the graph goes linear at small strain levels. Then, linearity breaks, and the nonlinear curve continues until the yield point. After the yield point, as noticed, strain hardening behavior starts, and large strain deformation occurs until the breaking point without necking. Elongation varies from nearly 250% to 450%. The chain microstructure of the Varioshore TPU filament (Colorfabb, Netherlands) allows this large deformation. Chain structure oriented along loading direction.

In Figure 3.1 (b), the effect of the nozzle temperature on the printing process can be easily observed. Although the mechanical properties of all specimens show similarities, the elongation rates, strain hardening rates, fraction stresses, and yield

stresses are different. Temperature affects the molecular structure of the material, and it causes gaps between the molecules at different levels at different temperatures. In other words, the Varioshore TPU filament (Colorfabb, Netherlands) is foaming in high temperatures. So, this affects the mechanical properties.

Figure 3.1 (c) and Figure 3.1 (d) show the effects of the nozzle temperatures on the mechanical properties and density of Varioshore TPU. The tensile strength and the elongation at break show similar characteristics, as seen in Figure 3.1 (b). There is a decreasing path of the elongation at break and the tensile strength. At 190°C, the tensile strength is 9.88 MPa while the elongation is 439.9%. Up to 220°C, there is a nearly linear drop line. After this drop, there is a brief rise at 235°C, the tensile stress increases to 5.81 MPa, and the elongation at break increases to 358.52%. Then, from 235°C to 250°C, the tensile stress decreased to 4.63 MPa and the elongation at break slightly decreased to 281.45%. The stress decreases nearly in linear path. This decrease might be the result of the foaming effect. When foaming increases with increasing printing temperature, and the stress decreases. The porous microstructure causes weaker specimens.

In Figure 3.1 (d), the densities of the tensile specimens are compared. The density of the tensile specimens shows quite similar behavior with tensile strength. Density at 190°C, 0.922g/mm^3 and it slightly decreased at 205°C. However, at 220°C there is a sharp drop. At 235°C, density slightly increased and at 250°C, there is drop again. The volume and the mass of the specimens are measured from the manufactured the tensile specimen. In other meaning, the geometrical expansion of filaments with the foaming effect is considered during the density calculation. The reason for the sharp drop at 220°C might be the filaments are expanded more than at lower temperatures. Therefore, the mass decreases with foaming and at the same time, the volume increases. In conclusion, density decreased dramatically.

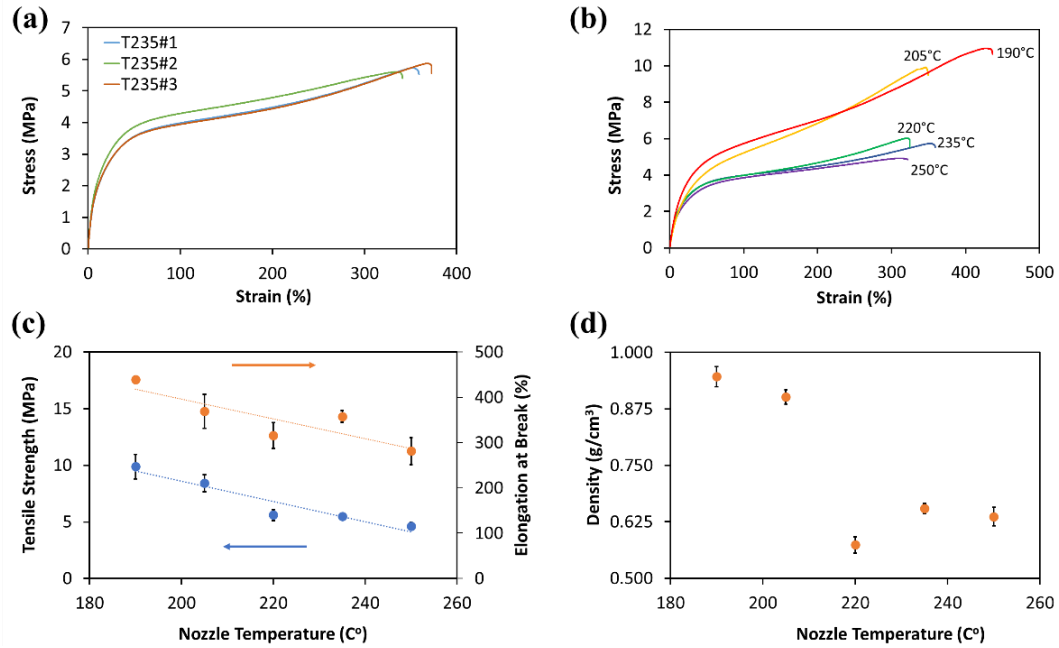

Figure 3.1 (a) Stress-Strain behavior of Varioshore TPU at extrusion temperature 235°C. (b) UTS vs. the nozzle temperature and elongation at break vs. the nozzle temperature. (c) Densities of dog bone specimens at different extrusion temperatures.

In Figure 3.2, SEM images of the tensile specimen are shown. As noticed, at 190°C nozzle temperature, the specimen has the lowest porosity. Separate filament layers can be easily observed. Similarly, at 205°C nozzle temperature, filament layers can be easily distinguished. However, at 220°C, 235°C and 250°C, the layers begin to unite and become a more porous structure. Layers could not be easily distinguished and at 235°C layers become almost one piece. Moreover, the porosity seems the highest at 235°C and 250°C among other temperatures. It is an expected result because of the foaming behavior of TPU Varioshore. The difference between 190°C and 220°C in Figure 3.2 supports the density drop in Figure 3.1 (d).

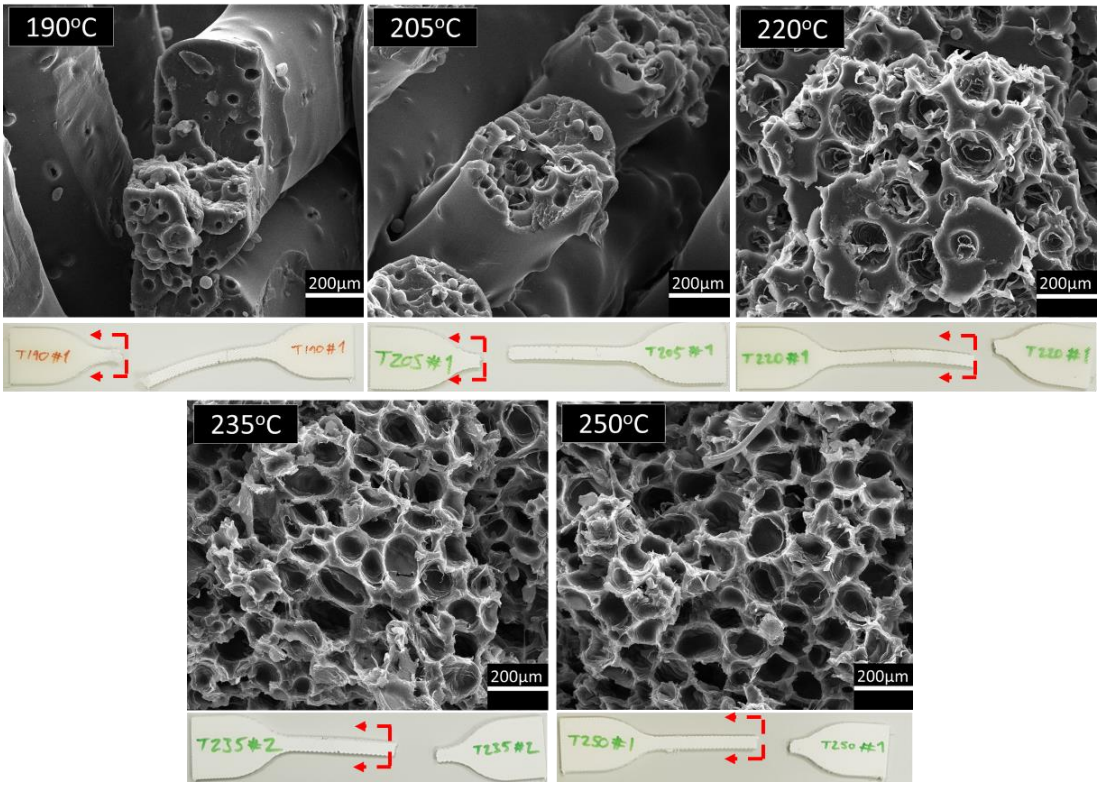

Figure 3.2 At the top: SEM images of the specimens. At the bottom: Photographs indicating the viewing directions of the SEM images. The images on the left and the right correspond to 190°C and 235°C extrusion temperatures, respectively.

3.2 Compression Testing

The Varioshore TPU filament was applied the compression test in five different temperature groups from 190°C to 250°C for a better understanding of the compression characteristics and the effect of the nozzle temperature during and after the printing process.

The engineering stress-strain curve of Varioshore TPU foam at 190°C for the compressive test is given in Figure 3.3 (a). The compressive test is performed for four groups of different extrusion temperatures. It can be observed that all specimens show similar characteristics in their temperatures as in Figure 3.3 (a); the specimen is manufactured at 190°C shows. The experiment was performed up to %40 strain level.

In Figure 3.3 (b), the levels of the compressive stresses by changing the printing nozzle temperatures can be observed. The highest compressive stress at 40% strain level belongs to 205 °C, and the lowest one belongs to 250°C.

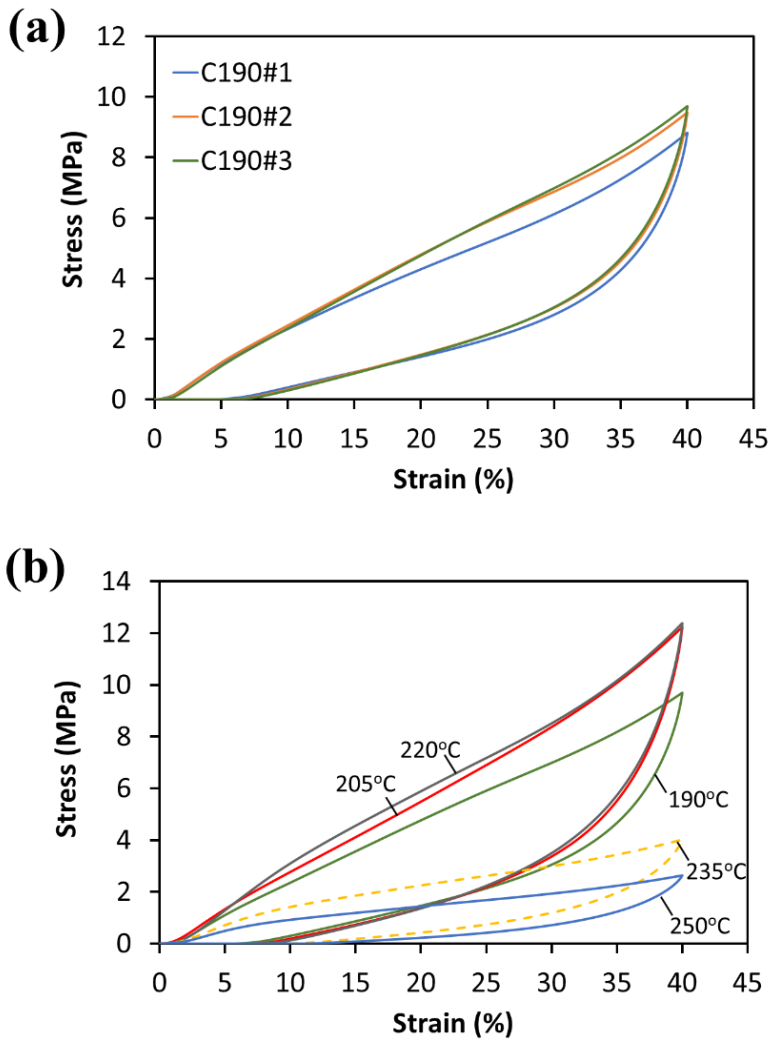

Figure 3.3 (a) Stress-Strain behavior of Varioshore TPU at extrusion temperature 190°C (b) Stress-Strain behavior comparison of Varioshore TPU at different extrusion temperatures.

In Figure 3.4, the compression stress levels at 40% strain are shown. The compression stress increases at the beginning from 190°C to 205°C. Stress level is nearly the same for 205°C and 220°C. Then, there is a critical drop at 235°C. From 235°C to 250°C, stress slightly decreased. On the contrary tensile test, the stress initially increased at the compression test. The reason might be the fusion between

layers. In other words, the printed layer overlaps the previous layer, and this overlap affects the density, eventually affecting the specimen's stress. However, after some critical temperature points, the porosity effect overcomes the fusion effect, and the density starts decreasing. It causes stress to drop at higher temperatures.

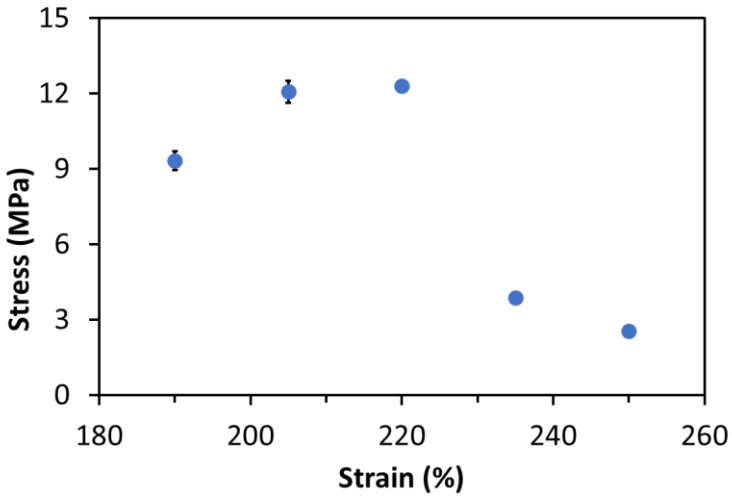

Figure 3.4 Compression stresses at 40% strain.

3.3 Honeycomb Compression Testing

The Varioshore TPU filament was applied the honeycomb compression testing in four different temperature groups from 190°C to 235°C for a better understanding of the compression characteristics of honeycombs and the effect of the nozzle temperature during and after the printing process.

In Figure 3.5 (a), it can be observed that stress-strain behavior of the honeycomb structure which is manufactured at 235°C nozzle temperature. In Figure 3.5 (a) inset, the elastic region of the stress-strain curve is zoomed in. The compressive characteristic is similar to elastomeric foam compressive behavior as expected [69]. In Figure 3.5 (b), the compressive behavior of the honeycomb can be observed in the stress-strain diagram. The elastic region is zoomed in Figure 3.5 (b) inset. It can be observed that at 235°C the honeycomb structure has the highest yield, the peak, and

the plateau stresses and at 190°C, it has the lowest one. The plateau stress, σ_{Pl}, and the yield stress, σ_y, calculations suggested by Gibson and Ashby are given in below [70].

$$\sigma_{Pl} = \frac{\int_{\varepsilon_y}^{\varepsilon_{cd}} \sigma(\varepsilon)\, d\varepsilon}{\varepsilon_{cd} - \varepsilon_y} \tag{3.1}$$

$$\frac{\sigma_{Pl}}{\sigma_y} = \frac{2}{3}\left(\frac{t}{l}\right)^2 \tag{3.2}$$

Here ε_{cd} and ε_y are the critical densification strain and the yield strain respectively in Equation 3.1. *t* is the thickness and *l* is the length of cell wall in the XY plane in Equation 3.2. These values are given in Appendix A.4.

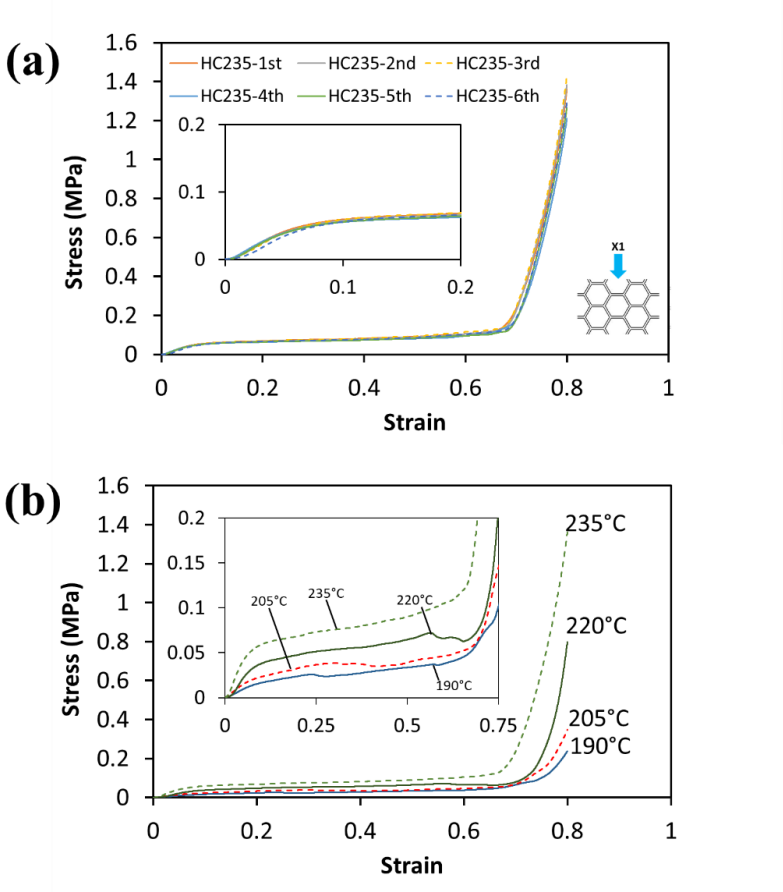

Figure 3.5 (a) Stress-Strain diagram of compressive test of the honeycomb structure which is manufactured at 235°C nozzle temperature. (b) Stress-Strain curve

comparison for honeycomb structure of Varioshore TPU at different nozzle temperatures.

In Table 3.1, it can be easily noticed that the lattice structures produced at 235°C nozzle temperature have higher relative density and the average relative densities varying in the nozzle temperatures in ascending order are 220°C, 205°C, 190°C, and 235°C. Relative density is a ratio between honeycomb density and solid density. The relative density calculation suggested by Gibson and Ashby is given in below [70]. In Equation 3.3, ρ_0 and ρ_s are honeycomb density and solid density respectively. These values are given in Appendix A.4. The densities are determined from the printed honeycomb structures. The honeycomb density represents the ratio between the honeycomb mass, and the fully closed assumed honeycomb volume. The solid density represents the base material density.

$$\frac{\rho_0}{\rho_s} = \frac{2}{\sqrt{3}}\left(\frac{t}{l}\right) \tag{3.3}$$

The relative density affects the densification strain and the plateau stress and eventually the yield stress and the yield strain. Because the densification strain is a function of the relative density [71]. The densification strain and the critical densification strain equations are given in Equation 3.4 and Equation 3.5 respectively, where ε_d is the densification strain, and α and D are experimental constants in Equation 3.4 and Equation 3.5. Gibson and Ashby suggest to take α as 1 and D as 1.4 [70]. In this study, α is accepted as 1, however, the critical densification strain is experimentally determined as shown in Figure 3.9.

$$\varepsilon_d = 1 - \alpha\frac{\rho_0}{\rho_s} \tag{3.4}$$

$$\varepsilon_{cd} = \varepsilon_d\left(1 - \frac{1}{D}\right) \tag{3.5}$$

The experimental studies in the literature show that with increasing the relative density, the peak stress, the yield stress, and the plateau stress increase, and the densification strain decrease [70], [72], [73]. However, in this study, this theory is

not completely applicable because 220°C does not completely fit the theory. To explain this unusual behavior, the given suggestion is that the mechanical properties of the lattice structures can be affected by the porosity of the honeycomb wall. In Figure 3.2, it was discussed that 235°C has one of the most porous microstructures and 190°C has the lowest. After 220°C printing temperature in Figure 3.2, the porosity level dramatically increased, and it affected the material behavior. It is expected that with increasing porosity, the strength of the material decreases and the stress level increases at the same strain level [70], [72]. However, with the increasing particle size, the strength of the lattice structure can be deteriorated [74], [75]. The low-density foams have weak walls at the microstructure level. In recent applications, these walls assumed constant width to simplify the analysis [76]. The wall thickness of the microstructure also affects the wall thickness of the honeycomb structure. In Figure 3.6, the variation in the wall thickness can be observed. This variation of the wall thickness is considerably large, and it affects the plateau stress and yield stress ratio in Equation 3.2 and the relative density in Equation 3.3. Also, it could be affecting the buckling of the honeycomb wall.

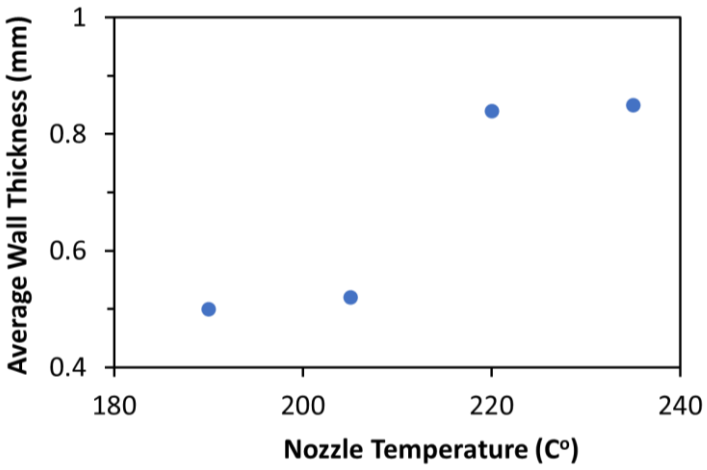

Figure 3.6 Average wall thickness vs. the nozzle temperature.

Figure 3.7 is a comparison graph of the energy absorption levels against the compression stress of TPU Varioshore lattice structures at different nozzle temperatures. The energy storage from the beginning of the loading up to the

densification is simply the area under the compressive stress-strain curve of the lattice structure and it is given in Equation 3.6 [70].

$$w = \int_0^{\varepsilon} \sigma(\varepsilon)\, d\varepsilon \tag{3.6}$$

Here σ and ε are the stress and the strain respectively in Equation 3.6. The volumetric energy absorption efficiency of a lattice structure is the energy absorption per unit volume which is expressed as the energy absorption divided by the stress level at the instant strain of the lattice structure [70], [72]. Energy absorption equation is given in Equation 3.7, and E and $\sigma(\varepsilon)$ are the energy absorption efficiency and the stress at related strain respectively in Equation 3.7.

$$E(\varepsilon) = \frac{\int_0^{\varepsilon} \sigma(\varepsilon)\, d\varepsilon}{\sigma(\varepsilon)} \times 100 \tag{3.7}$$

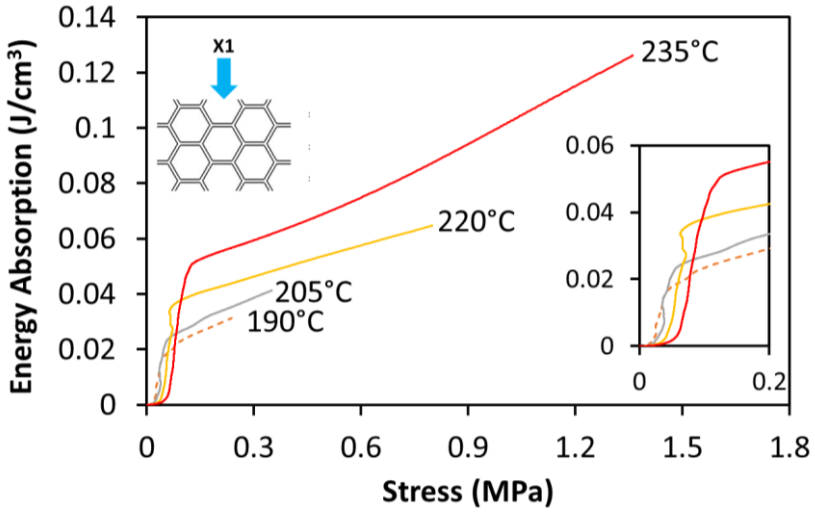

Figure 3.7 Energy Absorption-Stress comparison for honeycomb structure of Varioshore TPU at different nozzle temperatures.

In Figure 3.8, the maximum efficiency curves calculated by Equation 3.7 for the honeycomb structure at different nozzle temperatures are shown. The maximum energy absorption efficiency values for all nozzle temperatures are nearly %40 and efficiency percentages are close to each other.

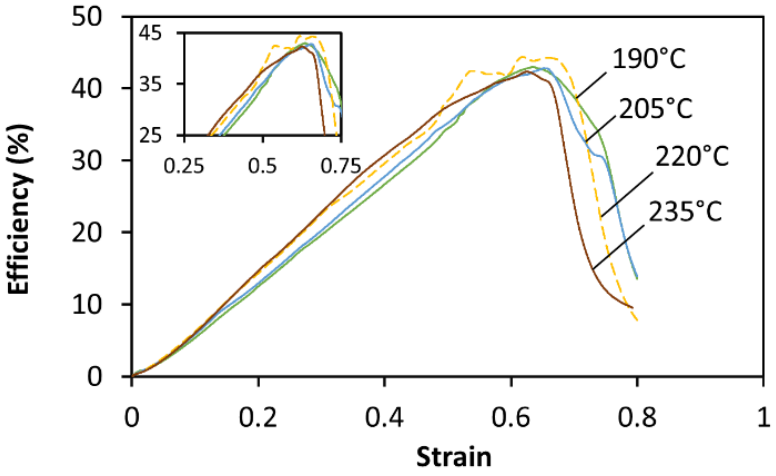

Figure 3.8 Efficiency comparison for honeycomb structure of Varioshore TPU at different nozzle temperatures.

Figure 3.9 shows the maximum efficiency, the peak stress, and the critical densification strain from the stress-strain graph of the honeycomb structure. E_{max} is the maximum efficiency and σ_p and ε_{cd} are the peak stress and the critical densification strain respectively. It can be noticed that although there is no negative value in the equation of efficiency, Equation 3.7, the efficiency decreases after a certain point. The reason is that the denominator increases faster than the numerator after it reaches maximum efficiency. The numerator is the area under the curve and the denominator is the stress value at the instant strain value. The area and the stress increase are nearly linear up to a certain strain value. However, after this strain value the stress start to increase faster than the energy absorption and the efficiency starts to decrease. The strain value where efficiency starts to decrease is called the critical densification strain value and the stress at this strain is called the peak stress. To calculate the critical densification strain value this method is used instead of Equation 3.5.

In Figure 3.9, the blue dashed line shows the behavior of ideal energy absorber like a sponge. The stress level increase initially at zero strain up to the peak stress. Then, stress stays constant up to 100% strain level where no longer can be compressed. For an ideal absorber, the efficiency follows a linear path, starting from 0 to 100%

efficiency at 100% strain level. For better understanding, the honeycomb test results can be compared with ideal absorber in Figure 3.9.

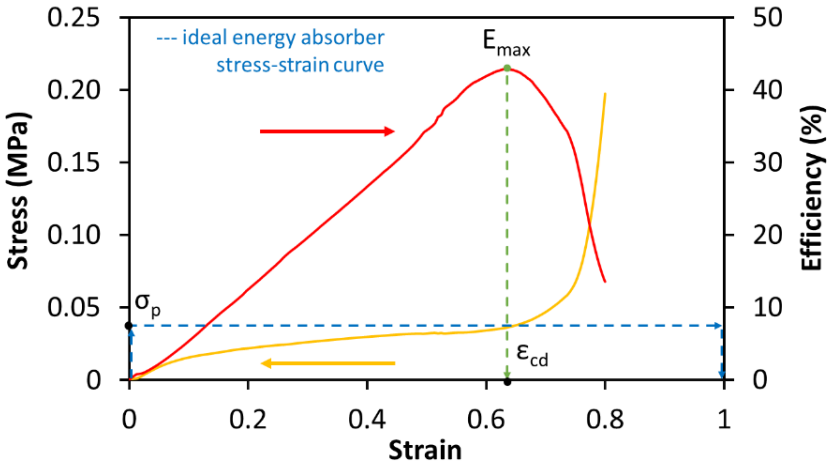

Figure 3.9 Stress and efficiency vs. strain for honeycomb structure at 190°C nozzle temperature.

Table 3.1 shows the summary of the mechanical properties of the honeycomb structures that are extruded at different nozzle temperatures. These values can be determined by the equations previously discussed; however, the experimental result can be different than the theoretical calculations. Therefore, experimental results are used to obtain the values in Table 3.1 as discussed. The relative density in Equation 3.3 calculated with the printed honeycomb density and the solid density. It is inversely proportion with the densification strain. They are tabulated in Table 3.1.

Figure 3.9 shows the experimental determination of the peak stress, the critical densification strain, and the maximum efficiency. This is how they were calculated in Table 3.1. Yield stress in Table 3.1, calculated from the point where the linearity breaks in the stress-strain curves of the honeycomb structures.

For each temperature level, Table 3.1 is detailed in Appendix A.3. The lower values in Table 3.1 for each temperature show the standard deviation. It can be easily noticed they are very small values, and the deviations show that the tests are consistent.

Table 3.1 Summary of Honeycomb Mechanical Properties.

Temperature (C°)	Maximum Efficiency (%)	Relative density Experimental (%)	Densification Strain (porosity)	Critical Densification Strain	Peak Stress (MPa)	Yield Stress (MPa)	Energy (J/cm^3)
190	40.088	17.695	0.823	0.634	0.041	0.016	0.016
	±1.37	±0.3	±0	±0.03	±0.01	±0	±0
205	42.364	17.156	0.828	0.604	0.044	0.021	0.019
	±0.85	±0.42	±0	±0.03	±0	±0	±0
220	47.530	17.012	0.830	0.640	0.070	0.038	0.033
	±3.75	±0.23	±0	±0.02	±0.01	±0	±0
235	41.642	27.040	0.730	0.629	0.108	0.055	0.045
	±1.2	±0.46	±0	±0.03	±0.01	±0	±0

CHAPTER 4

CONCLUSIONS AND FUTURE WORK

In this study, Varioshore TPU specimens that were produced by the FFF technique, were investigated to find out the mechanical properties of novel material Varioshore TPU at different geometries such as the tensile specimens, the compression specimens, and the lattice structures. During manufacturing, different nozzle temperatures were applied to activate foaming phenomena.

In the tensile testing, Varishore TPU showed the nonlinear hyperelastic curve for each temperature level. Tensile specimens elongated over 300% before failure. The material showed similar behavior at the same temperature. This showed the repeatability of the FFF technique for tensile specimens. Also, relatively lower temperatures showed similar characteristics. This was the reason that the foaming phenomena has not been activated at low temperatures. At high temperatures, foaming was activated and as a result of that tensile strength was downgraded.

Foaming phenomena and repeatability subjects were valid for the compression also. The compression specimens were compressed up to 40% of the initial height and recovered their deformation during the unloading.

The difference between the compression and the tensile test have been explained with the fusion effect between layers at relatively low temperatures. The fusion effect may not be effective for tensile specimens because of the narrow printing region. For the compression specimens, there was a larger region for printing. Also, the printing direction could be the reason for the difference because as mentioned before, all specimens were printed in the Z direction. In tensile test, load was applied in the X direction, yet, in the compression test, load was applied in the Z direction. For this reason, in lower temperatures, the compression specimens could be stronger.

For the lattice structure, the honeycomb structure was studied which is one of the most commonly used lattice structures in literature. Again, repeatability was shown for the honeycomb compression test. The energy absorption level of honeycomb varied with the foaming level. This was a result of the different nozzle temperatures as discussed. At higher relative density higher energy absorption was observed. In other words, when the porosity increased the absorber characteristic of honeycomb became better. Therefore, it was possible to achieve high energy absorption levels with the manipulation of the FFF printing parameter. FFF offered arrangeable parameters during manufacturing operations. Although foamed materials showed higher absorption levels, it could not be said that the most foamed material with 235^{o}C nozzle temperature was the most efficient. Efficiency was related to absorbed energy and stress level.

In this thesis study, five printing temperature levels were validated. The foaming phenomena of TPU and its effect on mechanical properties were studied. Foaming had a remarkable effect on the mechanical properties of TPU, and the energy absorption level of lattice structures. The temperature was used to activation of the foaming.

In the future, other parameters than the temperature of the printing process can be changed to observe differences. FFF gives a chance to interfere with the production process parameter. The printing speed can be investigated, and the study can be expanded by arranging the printing speed.

As lattice structure geometry, honeycomb geometry was chosen. In the future, another lattice structure model can be used to compare the energy absorption and the nozzle temperature effect. For example, cubic lattice, diamond lattice, triangular lattice or lattice structures with tailored cell geometries can be manufactured to obtain optimized geometry for the energy absorption.

In future work, closer temperatures can be considered as the nozzle temperatures to obtain the beginning temperature of the foaming and observe the temperature effect in more detail. Moreover, other parameters such as the feed rate, the nozzle moving

speed, the printing table temperature, or the infill density can be investigated to find out any effects of the foaming activation.

FEM analysis was not performed during the study. For a better understanding of structures FEM analysis and the material modeling can be performed. This study can also provide an effective route for designing impact-absorbing structures for the helmets and similar protective equipment.

REFERENCES

[1] BETTINA WARBURG, "Additive Manufacturing vs. Traditional Manufacturing," Polymer 207, Aug. 06, 2020.

[2] K. V. Wong and A. Hernandez, "A Review of Additive Manufacturing," *ISRN Mechanical Engineering*, vol. 2012, pp. 1–10, Aug. 2012, doi: 10.5402/2012/208760.

[3] S. H. Huang, P. Liu, A. Mokasdar, and L. Hou, "Additive manufacturing and its societal impact: a literature review," *Int J Adv Manuf Technol*, vol. 67, no. 5–8, pp. 1191–1203, Jul. 2013, doi: 10.1007/s00170-012-4558-5.

[4] H. Paris, H. Mokhtarian, E. Coatanéa, M. Museau, and I. F. Ituarte, "Comparative environmental impacts of additive and subtractive manufacturing technologies," *CIRP Annals*, vol. 65, no. 1, pp. 29–32, 2016, doi: 10.1016/j.cirp.2016.04.036.

[5] R. M. Mahamood', E. T. Akinlabi', M. Shukla, and S. Pityana, "Revolutionary Additive Manufacturing: An Overview," p. 19.

[6] V. Mazzanti, L. Malagutti, and F. Mollica, "FDM 3D Printing of Polymers Containing Natural Fillers: A Review of their Mechanical Properties," *Polymers*, vol. 11, no. 7, p. 1094, Jun. 2019, doi: 10.3390/polym11071094.

[7] W. R. Priedeman and P. W. Turley, "FDM® TECHNOLOGY PROCESS IMPROVEMENTS," p. 8.

[8] Crump S. S. (1992). Apparatus and method for creating three-dimensional objects (US5121329A). U.S. Patent and Trademark Office.

[9] B. Shaqour *et al.*, "Gaining a better understanding of the extrusion process in fused filament fabrication 3D printing: a review," *Int J Adv Manuf Technol*, vol. 114, no. 5–6, pp. 1279–1291, May 2021, doi: 10.1007/s00170-021-06918-6.

[10] S. Singh, G. Singh, C. Prakash, and S. Ramakrishna, "Current status and future directions of fused filament fabrication," *Journal of Manufacturing Processes*, vol. 55, pp. 288–306, Jul. 2020, doi: 10.1016/j.jmapro.2020.04.049.

[11] A. A. Rashid and M. Koç, "Fused Filament Fabrication Process: A Review of Numerical Simulation Techniques," *Polymers*, vol. 13, no. 20, p. 3534, Oct. 2021, doi: 10.3390/polym13203534.

[12] A. Dey, I. N. Roan Eagle, and N. Yodo, "A Review on Filament Materials for Fused Filament Fabrication," *JMMP*, vol. 5, no. 3, p. 69, Jun. 2021, doi: 10.3390/jmmp5030069.

[13] I. Gibson, D. Rosen, and B. Stucker, *Additive Manufacturing Technologies*. New York, NY: Springer New York, 2015. doi: 10.1007/978-1-4939-2113-3.

[14] K. S. Boparai, R. Singh, and H. Singh, "Development of rapid tooling using fused deposition modeling: a review," *Rapid Prototyping Journal*, vol. 22, no. 2, p. 19, 2016.

[15] A. A. Bakır, R. Atik, and S. Özerinç, "Mechanical properties of thermoplastic parts produced by fused deposition modeling:a review," *RPJ*, vol. 27, no. 3, pp. 537–561, Apr. 2021, doi: 10.1108/RPJ-03-2020-0061.

[16] S. C. Daminabo, S. Goel, S. A. Grammatikos, H. Y. Nezhad, and V. K. Thakur, “Fused deposition modeling-based additive manufacturing (3D printing): techniques for polymer material systems,” *Materials Today Chemistry*, vol. 16, p. 100248, Jun. 2020, doi: 10.1016/j.mtchem.2020.100248.
[17] R. J. Schaefer, “MECHANICAL PROPERTIES OF RUBBER,” p. 18.
[18] V. Gonca and Y. Shvabs, “DEFINITION OF POISSON’S RATIO OF ELASTOMERS,” *ENGINEERING FOR RURAL DEVELOPMENT*, p. 6.
[19] D. Koblar and M. Boltežar, “Evaluation of the Frequency-Dependent Young’s Modulus and Damping Factor of Rubber from Experiment and Their Implementation in a Finite-Element Analysis,” *Exp Tech*, vol. 40, no. 1, pp. 235–244, Feb. 2016, doi: 10.1007/s40799-016-0027-7.
[20] *Physicochemical Behavior and Supramolecular Organization of Polymers*. Dordrecht: Springer Netherlands, 2009. doi: 10.1007/978-1-4020-9372-2.
[21] H. F. Brinson and L. C. Brinson, *Polymer Engineering Science and Viscoelasticity*. Boston, MA: Springer US, 2015. doi: 10.1007/978-1-4899-7485-3.
[22] A. A. Bakır, R. Neshani, and S. Özerinç, “Mechanical Properties of 3D-Printed Elastomers Produced by Fused Deposition Modeling,” in *Fused Deposition Modeling Based 3D Printing*, H. K. Dave and J. P. Davim, Eds. Cham: Springer International Publishing, 2021, pp. 107–130. doi: 10.1007/978-3-030-68024-4_6.
[23] “Printability of elastomer latex for additive manufacturing or3D printing.pdf.”
[24] J. E. Mark, “6 - Thermoset Elastomers,” *Applied Plastics Engineering Handbook*, p. 17.
[25] “Journal of Polymer Science Part C Polymer Symposia - 1969 - Holden - Thermoplastic elastomers.pdf.”
[26] W. Zhai, J. Jiang, and C. B. Park, “A review on physical foaming of thermoplastic and vulcanized elastomers,” *Polymer Reviews*, vol. 62, no. 1, pp. 95–141, Jan. 2022, doi: 10.1080/15583724.2021.1897996.
[27] D. Whelan, “Thermoplastic Elastomers,” in *Brydson’s Plastics Materials*, Elsevier, 2017, pp. 653–703. doi: 10.1016/B978-0-323-35824-8.00024-4.
[28] P. P. Järvelä, “JOHANNA PAUKKUNEN FOAMING OF THERMOPLASTIC ELASTOMERS,” p. 78.
[29] H. Lee, R. Eom, and Y. Lee, “Evaluation of the Mechanical Properties of Porous Thermoplastic Polyurethane Obtained by 3D Printing for Protective Gear,” *Advances in Materials Science and Engineering*, vol. 2019, pp. 1–10, Dec. 2019, doi: 10.1155/2019/5838361.
[30] J. Wang *et al.*, “Research of TPU Materials for 3D Printing Aiming at Non-Pneumatic Tires by FDM Method,” *Polymers*, vol. 12, no. 11, p. 2492, Oct. 2020, doi: 10.3390/polym12112492.
[31] C. Ge, L. Priyadarshini, D. Cormier, L. Pan, and J. Tuber, “A preliminary study of cushion properties of a 3D printed thermoplastic polyurethane Kelvin foam,” *Packag. Technol. Sci.*, vol. 31, no. 5, pp. 361–368, May 2018, doi: 10.1002/pts.2330.

[32] H. B. Gunasekaran, S. Ponnan, N. Thirunavukkarasu, A. Laroui, L. Wu, and J. Wang, “Rapid Carbon Dioxide Foaming of 3D Printed Thermoplastic Polyurethane Elastomers,” *ACS Appl. Polym. Mater.*, vol. 4, no. 2, pp. 1497–1511, Feb. 2022, doi: 10.1021/acsapm.1c01846.
[33] Q. Chen, P. Cao, and R. C. Advincula, “Mechanically Robust, Ultraelastic Hierarchical Foam with Tunable Properties via 3D Printing,” *Adv. Funct. Mater.*, vol. 28, no. 21, p. 1800631, May 2018, doi: 10.1002/adfm.201800631.
[34] A. Pawar, G. Ausias, Y.-M. Corre, Y. Grohens, and J. Férec, “Mastering the density of 3D printed thermoplastic elastomer foam structures with controlled temperature,” *Additive Manufacturing*, vol. 58, p. 103066, Oct. 2022, doi: 10.1016/j.addma.2022.103066.
[35] M. G. M. Marascio, J. Antons, D. P. Pioletti, and P.-E. Bourban, “3D Printing of Polymers with Hierarchical Continuous Porosity,” *Adv. Mater. Technol.*, vol. 2, no. 11, p. 1700145, Nov. 2017, doi: 10.1002/admt.201700145.
[36] D. Valiulis and E. Jurkonis, “ADDITIVE MANUFACTURING BY 3D AND 4D PRINTING METHODS: A REVIEW OF MATERIALS, METHODS AND APPLICATIONS,” p. 11, 2020.
[37] A. Gleadall, D. Visscher, J. Yang, D. Thomas, and J. Segal, “Review of additive manufactured tissue engineering scaffolds: relationship between geometry and performance,” *Burns & Trauma*, vol. 6, Dec. 2018, doi: 10.1186/s41038-018-0121-4.
[38] M. Nofar, J. Utz, N. Geis, V. Altstädt, and H. Ruckdäschel, “Foam 3D Printing of Thermoplastics: A Symbiosis of Additive Manufacturing and Foaming Technology,” *Advanced Science*, vol. 9, no. 11, p. 2105701, Apr. 2022, doi: 10.1002/advs.202105701.
[39] S. Guessasma, S. Belhabib, and H. Nouri, “Effect of printing temperature on microstructure, thermal behavior and tensile properties of 3D printed nylon using fused deposition modeling,” *J Appl Polym Sci*, vol. 138, no. 14, p. 50162, Apr. 2021, doi: 10.1002/app.50162.
[40] S.-K. Yeh, R. Rangappa, T.-H. Hsu, and S. Utomo, “Effect of extrusion on the foaming behavior of thermoplastic polyurethane with different hard segments,” *J Polym Res*, vol. 28, no. 7, p. 244, Jul. 2021, doi: 10.1007/s10965-021-02604-z.
[41] B. Hu, M. Li, J. Jiang, and W. Zhai, “Development of microcellular thermoplastic polyurethane honeycombs with tailored elasticity and energy absorption via CO2 foaming,” *International Journal of Mechanical Sciences*, vol. 197, p. 106324, May 2021, doi: 10.1016/j.ijmecsci.2021.106324.
[42] A. K. Singh, B. Patil, N. Hoffmann, B. Saltonstall, M. Doddamani, and N. Gupta, “Additive Manufacturing of Syntactic Foams: Part 1: Development, Properties, and Recycling Potential of Filaments,” *JOM*, vol. 70, no. 3, pp. 303–309, Mar. 2018, doi: 10.1007/s11837-017-2734-7.
[43] N. Ben Ali, M. Khlif, D. Hammami, and C. Bradai, “Mechanical and morphological characterization of spherical cell porous structures manufactured using FDM process,” *Engineering Fracture Mechanics*, vol. 216, p. 106527, Jul. 2019, doi: 10.1016/j.engfracmech.2019.106527.

[44] N. Gama, A. Ferreira, and A. Barros-Timmons, “3D Printed Thermoplastic Polyurethane Filled with Polyurethane Foams Residues,” *J Polym Environ*, vol. 28, no. 5, pp. 1560–1570, May 2020, doi: 10.1007/s10924-020-01705-y.
[45] “Adv Eng Mater - 2022 - Zhang - 3D-Printed Polyurethane Tissue-Engineering Scaffold with Hierarchical Microcellular Foam.pdf.”
[46] Q. Sun, G. M. Rizvi, C. T. Bellehumeur, and P. Gu, “Effect of processing conditions on the bonding quality of FDM polymer filaments,” *Rapid Prototyping Journal*, vol. 14, no. 2, pp. 72–80, Mar. 2008, doi: 10.1108/13552540810862028.
[47] C. Hohimer, J. Christ, N. Aliheidari, C. Mo, and A. Ameli, “3D printed thermoplastic polyurethane with isotropic material properties,” presented at the SPIE Smart Structures and Materials + Nondestructive Evaluation and Health Monitoring, Portland, Oregon, United States, Apr. 2017, p. 1016511. doi: 10.1117/12.2259810.
[48] E. Heiml, A. Hössinger-Kalteis, and Z. Major, “Experimental characterization of 3D printed cellular structures,” *Materials Today: Proceedings*, vol. 62, pp. 2528–2532, 2022, doi: 10.1016/j.matpr.2022.03.124.
[49] J. Yao, M. R. Barzegari, and D. Rodrigue, “Polyethylene Foams Produced under a Temperature Gradient with Expancel and Blends Thereof,” *Cellular Polymers*, vol. 29, no. 5, pp. 259–282, Sep. 2010, doi: 10.1177/026248931002900501.
[50] A. Bezazi and F. Scarpa, “Mechanical behaviour of conventional and negative Poisson’s ratio thermoplastic polyurethane foams under compressive cyclic loading,” *International Journal of Fatigue*, vol. 29, no. 5, pp. 922–930, May 2007, doi: 10.1016/j.ijfatigue.2006.07.015.
[51] N. Gama, A. Ferreira, and A. Barros-Timmons, “Polyurethane Foams: Past, Present, and Future,” *Materials*, vol. 11, no. 10, p. 1841, Sep. 2018, doi: 10.3390/ma11101841.
[52] C. Ge, S. Wang, W. Zheng, and W. Zhai, “Preparation of microcellular thermoplastic polyurethane (TPU) foam and its tensile property,” *Polym Eng Sci*, vol. 58, no. S1, pp. E158–E166, May 2018, doi: 10.1002/pen.24813.
[53] S. R. G. Bates, I. R. Farrow, and R. S. Trask, “3D printed polyurethane honeycombs for repeated tailored energy absorption,” *Materials & Design*, vol. 112, pp. 172–183, Dec. 2016, doi: 10.1016/j.matdes.2016.08.062.
[54] E. O. Bachtiar *et al.*, “3D printing and characterization of a soft and biostable elastomer with high flexibility and strength for biomedical applications,” *Journal of the Mechanical Behavior of Biomedical Materials*, vol. 104, p. 103649, Apr. 2020, doi: 10.1016/j.jmbbm.2020.103649.
[55] C. Zhang and M. R. Kessler, “Bio-based Polyurethane Foam Made from Compatible Blends of Vegetable-Oil-based Polyol and Petroleum-based Polyol,” *ACS Sustainable Chem. Eng.*, vol. 3, no. 4, pp. 743–749, Apr. 2015, doi: 10.1021/acssuschemeng.5b00049.
[56] A. R. Damanpack, A. Sousa, and M. Bodaghi, “Porous PLAs with Controllable Density by FDM 3D Printing and Chemical Foaming Agent,” *Micromachines*, vol. 12, no. 8, p. 866, Jul. 2021, doi: 10.3390/mi12080866.

[57] Á. Kmetty, K. Litauszki, and D. Réti, “Characterization of Different Chemical Blowing Agents and Their Applicability to Produce Poly(Lactic Acid) Foams by Extrusion,” *Applied Sciences*, vol. 8, no. 10, p. 1960, Oct. 2018, doi: 10.3390/app8101960.
[58] W. J. Choi *et al.*, “Rapid development of dual porous poly(lactic acid) foam using fused deposition modeling (FDM) 3D printing for medical scaffold application,” *Materials Science and Engineering: C*, vol. 110, p. 110693, May 2020, doi: 10.1016/j.msec.2020.110693.
[59] E. Williams, S. Long, M. Tatum, D. D. Anderson, and G. Thomas, “Designing a 3D Printed Bone Simulant for Wire Navigation Training,” in *2021 Design of Medical Devices Conference*, Minneapolis, MN, USA, Apr. 2021, p. V001T01A002. doi: 10.1115/DMD2021-1034.
[60] İ. Özsoykal, R. B. Husemoglu, and A. Yurt, “Radiological Evaluation of the Effects of Printing Parameters on 3D Printed Cylindrical LW-PLA Samples: Preliminary Results,” *Journal of Medical Innovation and Technology*, Jan. 2022, doi: 10.51934/jomit.1037540.
[61] C. Lancea *et al.*, “Design and additive manufacturing of brushless electric motor components,” *MATEC Web Conf.*, vol. 343, p. 01007, 2021, doi: 10.1051/matecconf/202134301007.
[62] O. Faruk and M. Sain, “Continuous Extrusion Foaming of Lignin Enhanced Thermoplastic Polyurethane (TPU),” *j biobased mat bioenergy*, vol. 7, no. 3, pp. 309–314, Jul. 2013, doi: 10.1166/jbmb.2013.1365.
[63] X. Chen and S. Lee, “Physical Property of 3D-Printed N-Pointed Star-Shaped Outsole Prepared by FDM 3D Printer Using the Lightweight TPU,” *Polymers*, vol. 14, no. 15, p. 3189, Aug. 2022, doi: 10.3390/polym14153189.
[64] X. Chen and S. Lee, “Morphology and Compressive Property of 3D-printed 3-pointed Star Shape Prepared Using Lightweight Thermoplastic Polyurethane,” *Fibers Polym*, vol. 23, no. 7, pp. 1779–1788, Jul. 2022, doi: 10.1007/s12221-022-4833-5.
[65] E. J. Parry, J. M. Best, and C. E. Banks, “Three-dimensional (3D) scanning and additive manufacturing (AM) allows the fabrication of customised crutch grips,” *Materials Today Communications*, vol. 25, p. 101225, Dec. 2020, doi: 10.1016/j.mtcomm.2020.101225.
[66] D11 Committee, “Test Methods for Vulcanized Rubber and Thermoplastic ElastomersTension,” ASTM International. doi: 10.1520/D0412-16R21.
[67] D11 Committee, “Test Methods for Rubber Properties in Compression,” ASTM International. doi: 10.1520/D0575-91R18.
[68] “TDS_E_ColorFabb_varioShore_TPU.pdf.”
[69] “Cellular Solids Structure and Properties (Cambridge Solid State Science Series) (Lorna J. Gibson, Michael F. Ashby) (z-lib.org).pdf.”
[70] L. J. Gibson and M. F. Ashby, *Cellular Solids: Structure and Properties*, 2nd ed. Cambridge University Press, 1997. doi: 10.1017/CBO9781139878326.
[71] Q. M. Li, I. Magkiriadis, and J. J. Harrigan, “Compressive Strain at the Onset of Densification of Cellular Solids,” *Journal of Cellular Plastics*, vol. 42, no. 5, pp. 371–392, Sep. 2006, doi: 10.1177/0021955X06063519.

[72] F. N. Habib, P. Iovenitti, S. H. Masood, and M. Nikzad, “In-plane energy absorption evaluation of 3D printed polymeric honeycombs,” *Virtual and Physical Prototyping*, vol. 12, no. 2, pp. 117–131, Apr. 2017, doi: 10.1080/17452759.2017.1291354.
[73] I. Ivañez, L. M. Fernandez-Cañadas, and S. Sanchez-Saez, “Compressive deformation and energy-absorption capability of aluminium honeycomb core,” *Composite Structures*, vol. 174, pp. 123–133, Aug. 2017, doi: 10.1016/j.compstruct.2017.04.056.
[74] D. Ghosh, N. Dhavale, M. Banda, and H. Kang, “A comparison of microstructure and uniaxial compressive response of ice-templated alumina scaffolds fabricated from two different particle sizes,” *Ceramics International*, vol. 42, no. 14, pp. 16138–16147, Nov. 2016, doi: 10.1016/j.ceramint.2016.07.131.
[75] M. Banda and D. Ghosh, “Effects of porosity and strain rate on the uniaxial compressive response of ice-templated sintered macroporous alumina,” *Acta Materialia*, vol. 149, pp. 179–192, May 2018, doi: 10.1016/j.actamat.2018.02.027.
[76] N. Mills, *Polymer foams handbook: engineering and biomechanics applications and design guide*. Elsevier, 2007.

APPENDICES

A.1 Printing Parameters

Table A.1 Detailed Table of Printing Parameters.

Sample ID	T190	T205	T220	T235	C190	C205	C220	C235	190HC	205HC	220HC	235HC
Infill Percentage	100%	100%	100%	100%	100%	100%	100%	100%	100%	100%	100%	100%
Infill Direction	±45°	±45°	±45°	±45°	±45°	±45°	±45°	±45°	±45°	±45°	±45°	±45°
Wall Thickness	0	0	0	0	0.2	0.2	0.2	0.2	0	0	0	0
Number of Wall	0	0	0	0	1	1	1	1	0	0	0	0
Bed Temperature	40	40	40	40	40	40	40	40	40	40	40	40
Nozzle Temperature	190	205	220	235	190	205	220	235	190	205	220	235
Printing Speed	30	30	30	30	30	30	30	30	30	30	30	30
Layer Thickness	0.2	0.2	0.2	0.2	0.2	0.2	0.2	0.2	0.2	0.2	0.2	0.2
Nozzle Diameter	0.4	0.4	0.4	0.4	0.4	0.4	0.4	0.4	0.4	0.4	0.4	0.4
Filament Diameter	2.85	2.85	2.85	2.85	2.85	2.85	2.85	2.85	2.85	2.85	2.85	2.85

A.2 Honeycomb compression test direction comparison

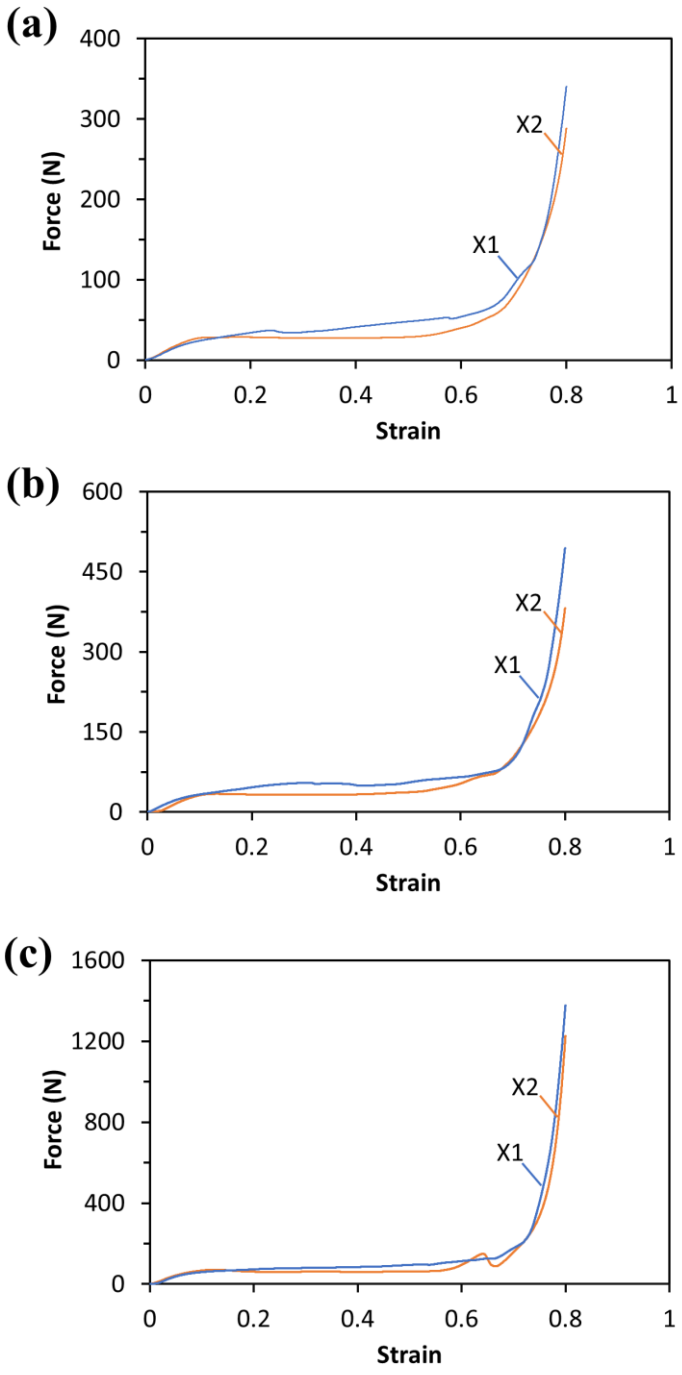

Figure A.2 Comparison of honeycomb compression test direction (a) 190°C (b) 205°C (c) 220°C.

A.3 Honeycomb Compression Properties

Table A.3 Detailed honeycomb compression properties.

Sample Name	Maximum Efficiency (%)	Relative density Experimental (%)	Densification Strain (porosity)	Critical Densification Strain	Peak Stress (MPa)	Yield Stress of HC (MPa)	Energy (J/cm3)
HC190#1	39.825	17.939	0.821	0.642	0.043	0.016	0.017
HC190#2	38.884	17.998	0.820	0.620	0.039	0.015	0.015
HC190#3	39.396	17.853	0.821	0.688	0.051	0.016	0.020
HC190#4	40.170	17.351	0.826	0.628	0.038	0.015	0.015
HC190#5	43.013	17.217	0.828	0.635	0.036	0.015	0.015
HC190#6	39.241	17.809	0.822	0.591	0.037	0.016	0.014
HC205#1	41.252	17.546	0.825	0.555	0.042	0.021	0.018
HC205#2	42.033	17.763	0.822	0.598	0.046	0.021	0.019
HC205#3	42.643	17.125	0.829	0.616	0.048	0.022	0.020
HC205#4	42.812	16.715	0.833	0.653	0.047	0.019	0.020
HC205#5	41.623	17.203	0.828	0.581	0.041	0.020	0.017
HC205#6	43.819	16.582	0.834	0.623	0.042	0.021	0.018
HC220#1	53.457	17.230	0.828	0.659	0.063	0.036	0.034
HC220#2	41.821	17.195	0.828	0.661	0.086	0.039	0.036
HC220#3	49.461	16.888	0.831	0.628	0.064	0.038	0.031
HC220#4	46.936	16.648	0.834	0.650	0.068	0.036	0.032
HC220#5	44.390	16.837	0.832	0.618	0.069	0.037	0.031
HC220#6	49.118	17.277	0.827	0.624	0.068	0.040	0.033
HC235#1	42.317	27.267	0.727	0.625	0.109	0.057	0.046
HC235#2	40.783	27.228	0.728	0.649	0.116	0.056	0.047
HC235#3	39.923	27.614	0.724	0.633	0.121	0.057	0.048
HC235#4	42.302	26.213	0.738	0.568	0.087	0.053	0.037
HC235#5	43.541	26.685	0.733	0.644	0.102	0.054	0.044
HC235#6	40.983	27.233	0.728	0.654	0.115	0.053	0.047

A.4 Honeycomb Parameters

Table A.4 Average honeycomb parameters.

Temperature (C^{o})	**Average wall thickness, *t* (mm)**	**Average wall length, *l* (mm)**	**Solid density (g/mm^3)**	**Honeycomb density (g/mm^3)**
190	0.5	3.54	0.915	0.162
205	0.52	3.51	0.972	0.167
220	0.84	3.45	0.972	0.165
235	0.85	3.52	0.551	0.169